



Preparation, structural characterization, voltammetry and Hirshfeld surface analysis of homoleptic iron(III) thiosemicarbazone complexes

Waleska R. P. Costa¹ · Rafael A. C. Souza¹ · Victor M. Deflon² · Carolina G. Oliveira¹

Received: 30 March 2020 / Accepted: 29 May 2020
© Springer Nature Switzerland AG 2020

Abstract

Reactions of FeSO₄ precursor with thiosemicarbazones Hatc-R, where R is ethyl (Et) or phenyl (Ph), led to the formation of homoleptic iron(III) complexes of the type [Fe(atc-R)₂]HSO₄. The characterization of the compounds was performed by spectroscopy techniques, such as FTIR, UV–Vis, besides elemental analysis, conductometry, voltammetry and magnetic susceptibility measurement. The crystalline structure of [Fe(atc-Ph)₂]HSO₄·H₂O was determined by single-crystal X-ray diffraction and revealed the oxidation of the Fe(II) centre to Fe(III) upon complexation of the monoanionic *N,N,S*-tridentate thiosemicarbazonate ligands. The magnetic susceptibility results showed the paramagnetic property of the iron(III) complexes in the extension of 1 unpaired electron. The electrochemical analyses showed a nearly reversible process of the iron complex, which is slightly influenced by the peripheral substituent groups at the *N*(4) position of the atc-R¹⁻ ligands. Hirshfeld surface analysis revealed that the supramolecular structure of [Fe(atc-Ph)₂]HSO₄·H₂O is stabilized mainly by H···H, C···H/H···C and O···H/H···O interactions.

Introduction

Transition metal complexes have many applications in distinct areas of inorganic and bioinorganic chemistry such as catalysis, luminescence, sensors and biological systems [1–4]. Indeed, numerous metal ions of the first transition series are present in a variety of metalloprotein and are essential to biological system functions. Copper(II) complexes, for instance, play numerous catalytic processes in

living organisms through electron transfer reactions [5] and have been extensively studied because of its biologically relevant redox properties [6], as also noted for complexes containing iron [7]. The complex properties are largely ligand dependent. For this reason, it is important to prepare efficient, flexible and versatile binding systems. The number and arrangement of donor atoms normally determine how the organic molecules coordinate to the metal centre.

Thiosemicarbazones (TSCs), a class of ligands containing nitrogen and sulphur donor atoms, have gained attention over the last decades in the main research areas of coordination chemistry [8, 9]. The potent chelator feature of TSCs is based on their chemical versatility, which provides variable binding modes and structural diversity that depends on the covalent sites number [10]. The ability of TSCs to form new metal complexes is well demonstrated in the literature with plenty of metal ions, including manganese(II) [11], copper(II) [12], zinc(II) [13], cobalt(III) [14], palladium(II) [15] and platinum(II) [16, 17].

Iron ion is of great relevance in life processes. In chemistry, iron compounds have been developed to be found in several applications, such as hydrogen evolution reaction [18, 19] and analytical methods [20], especially due to its electrochemical stability and reversibility. In the bioinorganic field, iron(III) thiosemicarbazone-based complexes

Electronic supplementary material The online version of this article (<https://doi.org/10.1007/s11243-020-00404-w>) contains supplementary material, which is available to authorized users.

✉ Carolina G. Oliveira
carolina@ufu.br

Waleska R. P. Costa
waleskarpc@gmail.com

Rafael A. C. Souza
rafasouza27@hotmail.com

Victor M. Deflon
deflon@iqsc.usp.br

¹ Institute of Chemistry, Federal University of Uberlândia, 38400-902 Uberlândia, Brazil

² São Carlos Institute of Chemistry, University of São Paulo, 13560-970 São Carlos, Brazil

have demonstrated applications as a potent tumour growth inhibitor [21] and antibacterial agents [22–24].

In the previous work, we investigated the structures and biological properties of some thiosemicarbazone ligands and their Mn(II) [11], Co(III) [14] and Zn(II) [13] complexes. In the present article, a new synthetic route is described to obtain ionic Fe(III) thiosemicarbazone compounds. We have explored the structural characterization, spectral and electrochemical properties. Besides that, the crystal structure of the bis(2-acetylpyridine-*N*(4)-phenylthiosemicarbazone) iron(III) hydrogenosulphate monohydrate ($2 \cdot \text{H}_2\text{O}$) was determined by X-ray diffraction and analysed by Hirshfeld surfaces to evaluate the intermolecular interactions in the crystalline structure and the effect of counter anion and water molecule to the crystal packing behaviour.

Experimental

Materials and methods

2-Acetylpyridine, 4-ethyl-3-thiosemicarbazide, 4-phenyl-3-thiosemicarbazide and analytical reagent grade chemicals and solvents were obtained commercially and used without further purification. The ligands Hatc-Et and Hatc-Ph were prepared by refluxing equimolar ethanolic solutions containing the desired thiosemicarbazide and 2-acetylpyridine for 1 h, as described before [25]. FTIR spectra were measured as KBr pellets on a Shimadzu IR Prestige-21 spectrophotometer between 400 and 4000 cm^{-1} . Elemental analyses were determined using a Leco Instrument, model TruSpec CHNS-O. The conductivities of the complexes were measured in $1 \times 10^{-3} \text{ mol L}^{-1}$ in MeOH solutions using an Orion Star Series conductometer. UV–visible (UV–Vis) spectra were measured with a Shimadzu UV-1800 spectrophotometer in MeOH solutions. The electrochemical experiments were carried out at room temperature in dichloromethane containing 0.1 mol L^{-1} tetrabutylammonium perchlorate (PTBA) (Fluka Purum) as a supporting electrolyte, using an electrochemical analyser μ Autolab III. Cyclic voltammetry experiments were performed using a Pt wire as working electrode, a miniaturized Ag/AgCl as reference electrode and a Pt wire as counter electrode in a Metrohm DropSens μ STAT-I 400 s potentiostat controlled in a personal computer by the DropView 8400 software, carried out with a rate sweep of 100 mV s^{-1} . Magnetic susceptibilities were measured on a JOHNSON MATTHEY MSB balance at 298 K and converted into the corresponding molar susceptibilities in the usual way [26, 27]. Diamagnetic corrections, applied to the molar susceptibilities of the paramagnetic substances, are reported as χ_{diam} . The latter corrections were calculated using the standard Pascal's constants [26, 27].

Synthesis of the complexes $[\text{Fe}(\text{atc-R})_2]\text{HSO}_4$

The Fe(III) complexes were prepared by adding 0.25 mmol of $\text{FeSO}_4 \cdot 7\text{H}_2\text{O}$ to a solution containing 0.50 mmol of ligands Hatc-Et and Hatc-Ph dissolved in 15 mL of MeOH. The resulting solutions were stirred under reflux at $80 \text{ }^\circ\text{C}$ for 30 min. The dark brown solids precipitated during this time were filtered off, washed with *n*-hexane and dried under vacuum. Brown crystals were obtained by slow evaporation of the mother solution. The characterization of the iron compounds is in accordance with the previous work [28].

$[\text{Fe}(\text{atc-Et})_2]\text{HSO}_4 \cdot 2\text{H}_2\text{O}$ ($1 \cdot 2\text{H}_2\text{O}$): Colour: brown. Yield: 80% (100 mg). Anal. Calcd for $\text{C}_{20}\text{H}_{31}\text{N}_8\text{O}_6\text{S}_3\text{Fe}$ (631.55 g/mol) C, 38.04; H, 4.95; N, 17.74%. Found: C, 37.25; H, 4.81; N, 17.25. IV ($\nu_{\text{max}}/\text{cm}^{-1}$): 3194 $\nu(\text{N-H})$, 1587, 1568 $\nu(\text{C=N}) + \nu(\text{C=C})$, 1053 $\nu(\text{N-N})$, 773 $\nu(\text{C-S})$, 1114 $\nu(\text{SO})$. UV–Vis, MeOH solution concentration: $2.52 \times 10^{-5} \text{ M}$ [λ_{max} (ϵ , $\text{L mol}^{-1} \text{cm}^{-1}$): 364 nm (15,436); Molar conductivity (Λ_{m} in MeOH): $78.0 \mu\text{S cm}^{-1}$.

$[\text{Fe}(\text{atc-Ph})_2]\text{HSO}_4 \cdot \text{H}_2\text{O}$ ($2 \cdot \text{H}_2\text{O}$): Colour: brown. Yield: 82% (126.4 mg). Anal. Calcd for $\text{C}_{28}\text{H}_{29}\text{N}_8\text{O}_5\text{S}_3\text{Fe}$ (709.62 g/mol): C, 47.39; H, 4.12; N, 15.79%. Found: C, 47.81; H, 4.13; N, 15.67%. IV ($\nu_{\text{max}}/\text{cm}^{-1}$): 3190 $\nu(\text{N-H})$ 1598, 1548 $\nu(\text{C=N}) + \nu(\text{C=C})$, 1049 $\nu(\text{N-N})$, 743 $\nu(\text{C-S})$, 1155 $\nu(\text{SO})$. UV–Vis, MeOH solution concentration: $1.88 \times 10^{-5} \text{ M}$ [λ_{max} (ϵ , $\text{L mol}^{-1} \text{cm}^{-1}$): 387 nm (13,599); 254 nm (25,585). Molar conductivity ($1 \times 10^{-3} \text{ mol L}^{-1}$ in MeOH): $63.0 \mu\text{S cm}^{-1}$. μ_{eff} : 1.83BM.

X-ray crystallography

Crystals of $[\text{Fe}(\text{atc-Ph})_2]\text{HSO}_4 \cdot \text{H}_2\text{O}$ were grown by slow evaporation of the mother solution. The data collections were performed using Mo-K α radiation ($\lambda = 71.073 \text{ pm}$) on a Bruker APEX II Duo diffractometer. Standard procedures were applied for data reduction and absorption correction. The structure was solved with SHELXS97 [29] software using direct methods, and all non-hydrogen atoms were refined with anisotropic displacement parameters in SHELXL2018 [30]. The hydrogen atoms were calculated at idealized positions using the riding model option of SHELXL2018 [30]. Structural representations were drawn using ORTEP-3 [30] and MERCURY [31]. Table 1 presents more detailed information about the structure determination.

Hirshfeld surface (HS)

The Hirshfeld surfaces were generated with the Crystal Explorer 2.1 program [32]. The strength of interactions was calculated by Hirshfeld d_{norm} (normalized contact distance) surface. The 2D fingerprint plots were calculated in order

Table 1 Crystallographic data for $[\text{Fe}(\text{atc-Ph})_2]\text{HSO}_4\cdot\text{H}_2\text{O}$

CCDC number	1990298
Empirical formula	$\text{C}_{56}\text{H}_{57}\text{Fe}_2\text{N}_{16}\text{O}_9\text{S}_6$
Molecular weight	1410.24
Temperature/K	293(2) K
Wavelength/Å	0.71073
Crystal system	Triclinic
Space group	$P\bar{1}$
a (Å)	11.3370(14)
b (Å)	15.0745(18)
c (Å)	18.711(2)
α (°)	87.580(7)
β (°)	87.602(7)
γ (°)	75.613(7)
V (Å ³)	3093.0(6)
Z	4
Density (calculated)	1.514
Absorption coefficient	0.742 mm^{-1}
Crystal size/ mm^3	0.339 × 0.242 × 0.196
Theta range for data collection	1.74–25.39
Index ranges	−13 ← h ← 13, −17 ← k ← 17, −20 ← l ← 22
Reflections collected	31,439
Independent reflections	10,452
Absorption correction	Multiscan
$T_{\text{min}}/T_{\text{max}}$	0.6200/0.7452
Refinement method	Full-matrix least-squares on F^2
Final R indices [$I > 2\sigma(I)$]	$R_1 = 0.0661$, $wR_2 = 0.1625$
R indices (all data)	$R_1 = 0.1263$, $wR_2 = 0.1976$
Goodness of fit on F^2	1.031

to analyse the relative contribution of different intermolecular interactions of compound $[\text{Fe}(\text{atc-Ph})_2]\text{HSO}_4\cdot\text{H}_2\text{O}$. The d_{norm} , shape index, curvedness and electrostatic potential surfaces were mapped using a fixed colour scale of −0.5000 to 1.7000 a.u., −1.0000 to 1.0000 a.u., −4.0000 to 0.4000 a.u. and −0.0500 to 0.0500 a.u. The 2D fingerprint plots were displayed using d_e and d_i distance scales on the graph axes (0.4 to 3.0 Å). All hydrogen bond lengths were

automatically modified to typical standard neutron values (C–H of 1.083 Å).

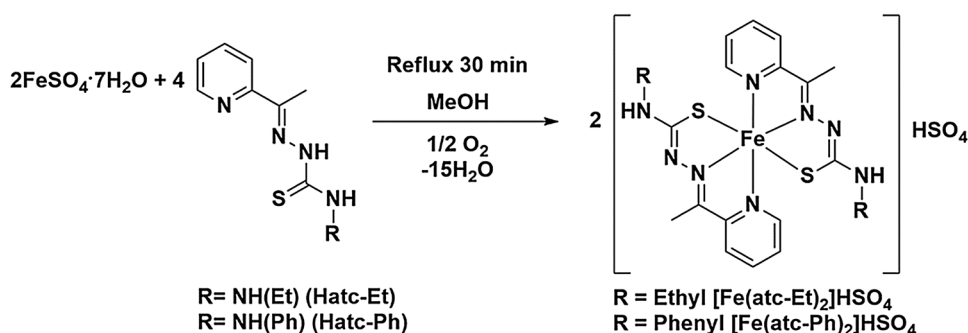
Results and discussion

Syntheses and characterization

Reactions of $\text{FeSO}_4\cdot 7\text{H}_2\text{O}$ with two equivalents of Hatc-R (R = ethyl or phenyl) in MeOH were stirred under reflux for 30 min resulting in dark brown precipitates of iron(III) complexes in good yields (Scheme 1) with slighted methods already described in the literature [28, 33]. The solids are soluble in DMSO and methanol but poorly soluble in CHCl_3 and CH_2Cl_2 .

The elemental analyses of both complexes are consistent with the formation of ionic complexes of the type $[\text{Fe}(\text{atc-R})_2]\text{HSO}_4$, in accordance with the molar conductivity values of 78 and 63 $\mu\text{S cm}^{-1}$ for compounds **1** $2\text{H}_2\text{O}$ and **2** H_2O , respectively, in the range of 1:1 electrolyte. The presence of the counterion was also confirmed by a strong band in the IR spectrum at 1155 cm^{-1} (for complex **1**, Fig. S1) corresponding to $\nu(\text{SO})$ stretching [34]. The N,N,S coordination mode in monoanionic form of both ligands was confirmed due to significant alterations in $\nu(\text{C}=\text{S})$, $\nu(\text{C}=\text{C} + \text{C}=\text{N})$ and $\nu(\text{N}-\text{H})$ stretches when compared with the free ligands. The same changes have been noted for similar complexes derived from thiosemicarbazone moieties [11, 14, 15]. In the spectra of the complexes **1** $2\text{H}_2\text{O}$ and **2** H_2O , the absorption related to the $\nu(\text{N}-\text{H})$ around 3300 cm^{-1} was not observed, as expected by the monodeprotonation of the ligands after complexation. The $\nu(\text{C}=\text{N})$ stretching band found close to 1579 cm^{-1} for the free ligands is observed in 1587–1600 cm^{-1} range for the complexes, indicating that the chelated rings formation causes a displacement of π electrons. The vibration attributed to the $\nu(\text{CS})$ stretch moves to lower frequencies (773 cm^{-1} for **1** and 743 cm^{-1} for **2** H_2O) after the coordination of the thiosemicarbazone ligand via sulphur atom, which is similar to other related complexes [35, 36].

The oxidation state of the iron central atom of the complexes was confirmed by the measurements of the magnetic

Scheme 1 Synthesis of the iron(III) complexes

susceptibility of $2 \cdot \text{H}_2\text{O}$. The value of magnetic moment measured at 25 °C was 1.83 BM, which is consistent with the calculated value of 1.73 BM, characteristic to d^5 low-spin Fe(III) complexes. This result is consistent with other low-spin thiosemicarbazone iron compounds [37], which agrees well with the bond lengths found for complex $2 \cdot \text{H}_2\text{O}$ latter characterized by X-ray diffraction.

The UV–Vis spectrum of $[\text{Fe}(\text{atc-Ph})_2]\text{HSO}_4$, recorded in methanol, showed two bands at 254 and 387 nm (Fig. S3). The band at higher energy (254 nm) consists of internal transitions $\pi \rightarrow \pi^*$ of the aromatic ring (substituted phenyl group), which is also observed in the absorption spectrum of the free ligand Hatc-Ph [38]. The absorption at 387 nm corresponds to a LMTC $\rho\pi(\text{S}) \rightarrow \sigma^* \text{Fe(III)}$, as well as verified for similar Fe(III) compounds [39].

Voltammetry analysis

Based on the feature of iron metal ion providing two stable oxidation states, the cyclic voltammetry (CV) of the complexes was studied. The experiments were performed in acetonitrile with tetra-*N*-butylammonium bromide, (NBu_4) Br, as supporting electrolyte. The cyclic voltammogram of complex $2 \cdot \text{H}_2\text{O}$ (Fig. 1, used as an example) shows a quasi-reversible single-electron redox process, as observed for similar Fe complex containing thiosemicarbazone [28]. The reversibility of the iron compounds between their oxidation states can suggest only very small changes in the coordination sphere of the complexes [33]. The electrochemical behaviour of the Fe(III) thiosemicarbazone complexes also proposed that their structures in solution are maintained.

The redox potential of the iron complexes prepared here was compared to other Fe compounds with structurally similar thiosemicarbazones (di-2-pyridyl ketone thiosemicarbazone—HDp4RT [21]), and chemical structures are

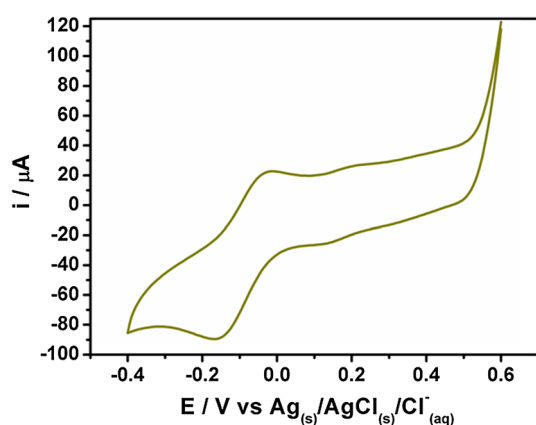


Fig. 1 Cyclic voltammogram of $[\text{Fe}(\text{atc-Ph})_2]\text{HSO}_4 \cdot \text{H}_2\text{O}$. The measurements were carried out in MeCN solution (0.05 M $[\text{NBu}_4]\text{Br}$) with a platinum electrode and scan rate 100 mV s^{-1}

shown in Fig. 2. The results are summarized in Table 2. The cathodic shift in the $\text{Fe}^{\text{III/II}}$ redox potentials of the $[\text{Fe}(\text{Dp4RT})_2]\text{ClO}_4$ complexes is visibly more positive than those found for the Fe complexes of the structurally related Hatc-R analogues [21, 28]. Through this information, it is possible to connect the cathodic process potential with the variation of C6 substituent from methyl (Hatc-R) to pyridine (HDp4RT). Interestingly, it can be seen that the potential related to the $\text{Fe}^{\text{III/II}}$ couple became more positive with strong electron-withdrawing of the exchange of pyridine substituent by methyl, following the order: $[\text{Fe}(\text{atc-R})_2]\text{HSO}_4 < [\text{Fe}(\text{atc-R})_2]\text{ClO}_4 < [\text{Fe}(\text{Dp4RT})_2]\text{ClO}_4$, showing their influence on the Fe(III) centre. The modifications of the R groups in the peripheral part of the ligand did not cause a significant alteration on the potential numbers of the complexes, as observed in Table 2 in which the Fe(III) compounds from the same series exhibited similar values of redox potentials. These remarkable observations may be attributed to the closer proximity of the substituent on C6 to the metal centre comparing to the substituent on *N*(4) atom by the R groups. This fact possibly confirms the greater sensitivity of the iron redox potential by closer modifications on the ligand moiety [33]. The different conditions under each voltammogram were performed, and the counterion of the compounds can result in few small differences in the potentials of the iron complexes from the same classes.

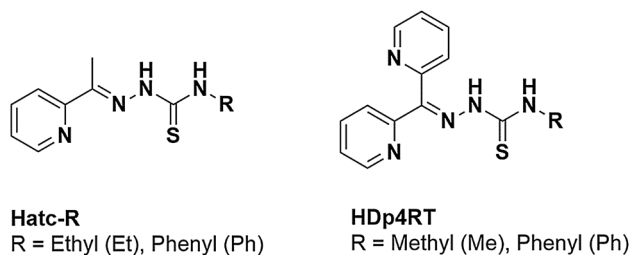


Fig. 2 Chemical structures of thiosemicarbazones Hatc-R and HDp4RT

Table 2 $\text{Fe}^{\text{III/II}}$ redox potentials (mV vs NHE) of the complex $[\text{Fe}(\text{atc-Ph})_2]\text{HSO}_4$, scan rate 100 mV s^{-1} (this work), in comparison with data reported by analogue Fe complexes of the type $[\text{Fe}(\text{atc-R})_2]\text{ClO}_4$ [33], $[\text{Fe}(\text{Dp4RT})_2]\text{ClO}_4$ [21]

Compounds	E° (mV vs NHS)
$[\text{Fe}(\text{atc-Ph})_2]\text{HSO}_4$	+34
$[\text{Fe}(\text{atc-Ph})_2]\text{ClO}_4^{\text{a}}$	+63
$[\text{Fe}(\text{atc-Et})_2]\text{ClO}_4^{\text{a}}$	+23
$[\text{Fe}(\text{Dp4eT})_2]\text{ClO}_4^{\text{b}}$	+173
$[\text{Fe}(\text{Dp4pT})_2]\text{ClO}_4^{\text{b}}$	+225

X-ray crystallography of 2·H₂O

Prism-shaped crystals were grown by slow evaporation of the mother solution of [Fe(atc-Ph)₂]HSO₄·H₂O (Fig. 3). Table 3 presents selected bond lengths and angles for compound 2·H₂O. The X-ray data showed that 2·H₂O crystallizes in the centrosymmetric space group P $\bar{1}$ of the triclinic system with four molecules by unit cell (Fig. 4a). In the asymmetric unit are detected two iron complex molecules, two hydrogen sulphate molecules and two water molecules. Table 1 presents more information about the structure determination of compound 2·H₂O. The thiosemicarbazone ligand binds to the iron atom as an *N,N,S*-chelate with single deprotonation upon complexation. The complex forms a distorted octahedral coordination geometry (Fig. 4b) with N(2A)–Fe(1)–N(6A) and N(1A)–Fe(1)–S(1A) angles of 173.40(19)° and 163.96(16)°, respectively.

The bond distances are in accordance with values found for similar Fe(III) compounds described in the literature [21, 28]. The distances Fe(1)–S(1A) and Fe(1)–S(2A), (2.2139(18) and 2.1976(16) Å, respectively) are visibly shorter than the same bonds in analogous Mn(II) compound [Mn(atc-Et)₂] (Mn–S(1A)/S(1B) [2.527(6)/2.521(5) Å]), due to the difference in oxidation state of each metal, Fe(III) and Mn(II) [11]. Otherwise, the bond distance for Fe(1)–S(1A) is similar to Co(1)–S(1A) [2.2185(10)] [14], and in this last case both metal ions have the same oxidation state. The C–S and C–N bond distances are consistent with single bond, 1.751(6) – 1.759(6) Å for two crystallographically independent molecules and double

Table 3 Selected bond lengths (Å) and angles (°) for complex 2·H₂O

Bond lengths (Å)			
Fe(1)–N(1A)	1.978(5)	Fe(2)–N(1B)	1.989(5)
Fe(1)–N(2A)	1.909(5)	Fe(2)–N(2B)	1.929(4)
Fe(1)–N(5A)	1.993(4)	Fe(2)–N(5B)	1.997(5)
Fe(1)–N(6A)	1.917(4)	Fe(2)–N(6B)	1.927(4)
Fe(1)–S(1A)	2.214(2)	Fe(2)–S(1B)	2.203(2)
Fe(1)–S(2A)	2.198(2)	Fe(2)–S(2B)	2.220(2)
S(1A)–C(8A)	1.751(6)	S(1B)–C(8B)	1.759(6)
Bond angles (°)			
N(2A)–Fe(1)–N(1A)	81.0(2)	N(2B)–Fe(2)–N(1B)	79.9(2)
N(2A)–Fe(1)–N(6A)	173.4(2)	N(2B)–Fe(2)–N(6B)	178.8(2)
N(6A)–Fe(1)–N(1A)	102.6(2)	N(6B)–Fe(2)–N(1B)	99.6(2)
N(1A)–Fe(1)–S(1A)	164.0(2)	N(1B)–Fe(2)–S(1B)	163.4(1)

bonds 1.312(8) – 1.309(7), correspondingly. The N–N, C(5A)–C(6A) and C(6A)–C(7A) bonds are also similar to values observed in other compounds [40]. Also, it was observed that the Fe(1)–S(1A and 2A), Fe(1)–N(2A and 6A) bond lengths (around 2.22 Å and 1.91 Å, respectively) are consistent with other low-spin Fe(III) complexes found in the literature [41]. On the other hand, the bond distances reported by Zhao and collaborators on high spin Fe(III) complexes of 5-bromosalicylaldehyde (pyridin-2-yl)hydrazone and 5-bromosalicylaldehyde thiosemicarbazone show Fe–S distance much longer coordinated [2.4093(14)] as well as the Fe bonded to imine nitrogen [2.157(3)] [42].

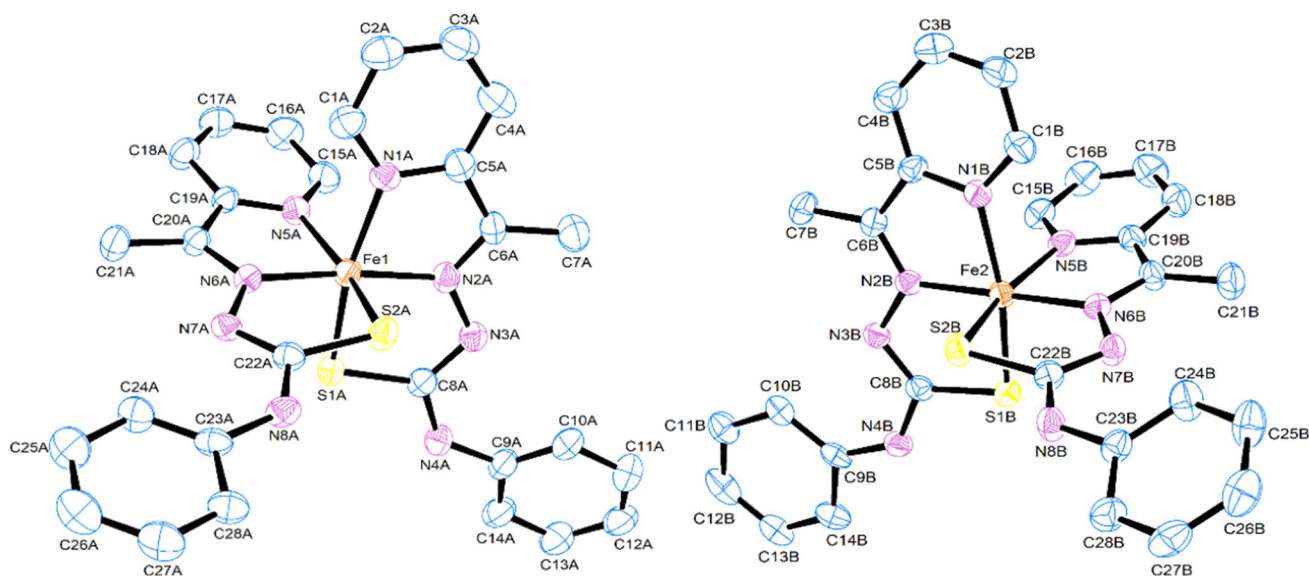
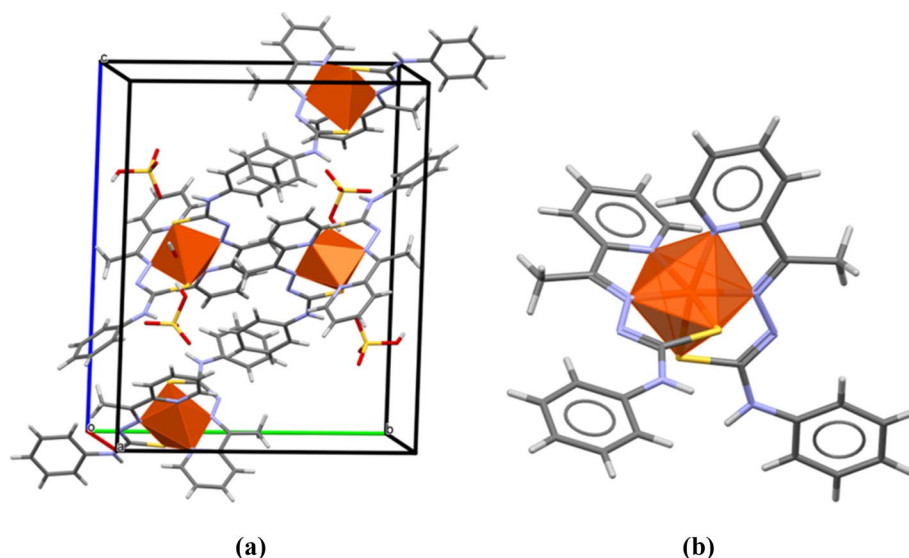


Fig. 3 ORTEP view of compound 2·H₂O with atom-numbering and displacement ellipsoids drawn with 30% probability level. For clarity, hydrogen atoms and HSO₄[−] counterion have been omitted. Crystal

structure of one molecule (labelled as A) of the asymmetric unit of 2·H₂O. Hydrogen atoms and HSO₄[−] counterion have been omitted for clarity

Fig. 4 **a** A view of the unit cells of $2 \cdot \text{H}_2\text{O}$ along the b axis and **b** molecular structure with the geometry of the Fe atom



By analysing the planarity of the ligands in the asymmetric unit of the $[\text{Fe}(\text{atc-Ph})_2]\text{HSO}_4 \cdot \text{H}_2\text{O}$, it is possible to verify the existence of two planes. The first plane is formed by the portion of the ligands including N(1A), C(1A), C(2A), C(3A), C(4A), C(5A), C(6A), C(7A), N(2A), N(3A), C(8A), S(1A) and N(4A) atoms with a RMS angle deviation of 0.176 \AA . The other plane starts at N8A atom and is extended across the pyridine group (RMSD = -0.272 \AA). The atoms related to the phenyl group from C(9A) to C(14A) and C(23A) to C(28A) have a high planarity, since the deviation from the RMS value is very close to zero (ca. 0.0085 \AA). The dihedral angle between both planes is 87.68° . The torsion angles around the N(4A)–C(9A) and N(8A)–C(23A) (ca. 11.85° , respectively) describe the conformation of the main plan in relation to phenyl rings.

The crystal packing of $2 \cdot \text{H}_2\text{O}$ exhibits seven C–H \cdots N (Fig. 5a, b), two O–H \cdots S, two C–H \cdots O, one O–H \cdots O and one N–H \cdots O intramolecular interaction, four C–H \cdots O, three N–H \cdots O, two O–H \cdots O and one N–H \cdots S intermolecular interactions (Fig. S4). In addition, there are two C–H \cdots π interactions. All interactions are summarized in Table S4. In addition, the crystalline structure is stabilized

by intermolecular hydrogen interactions between NH groups and water molecules, [N(4A)–H(4A) \cdots O(2W)], among hydrogen sulphate ions molecules [O(6)–H(6A) \cdots O(3), O(6)–H(6A) \cdots S(5)] and water molecules with hydrogen sulphate ions [O(1W)–H(11W) \cdots S(2B)] (Fig. 6). Due to the plenty variety of hydrogen bonds and tetrahedral geometry showed by hydrogen sulphate ion, those bonds have diverse directions. There are also three dimers in the crystal packing: one dimer between the compound and the hydrogen sulphate ion [N(8B)–H(8B) \cdots O2, C(28B)–H(28B) \cdots O3] giving rise to $R_2^2(8)$ ring motifs [43], one dimer between the water and the hydrogen sulphate ion [O(2W)–H(22W) \cdots O(5), O(2W)–H(22W) \cdots O(8)] giving rise to $R_1^2(4)$ ring motifs and one dimer between the compound, water and the hydrogen sulphate ion [N(4A)–H(4A) \cdots O(2W), O(2W)–H(22W) \cdots O(8), C(14A)–H(14A) \cdots O8] giving rise to $R_2^2(8)$ ring motifs.

Hirshfeld Surface Analysis of $2 \cdot \text{H}_2\text{O}$

The Hirshfeld surface (HS) analysis provides an understanding of interactions in the formation of the supramolecular

Fig. 5 Intramolecular interaction in $2 \cdot \text{H}_2\text{O}$ for **a** molecule A and **b** molecule B

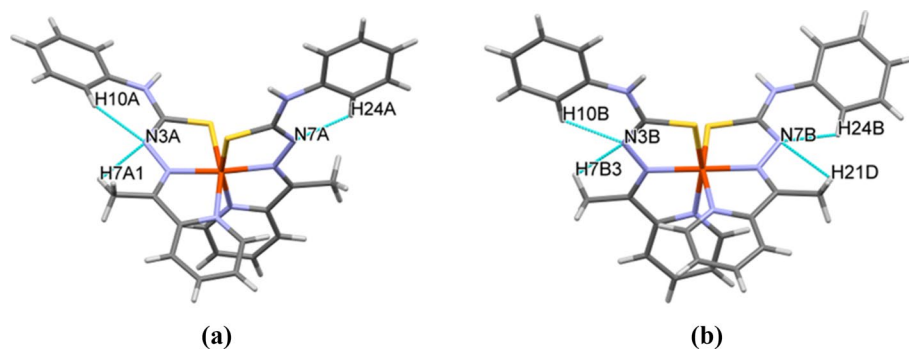
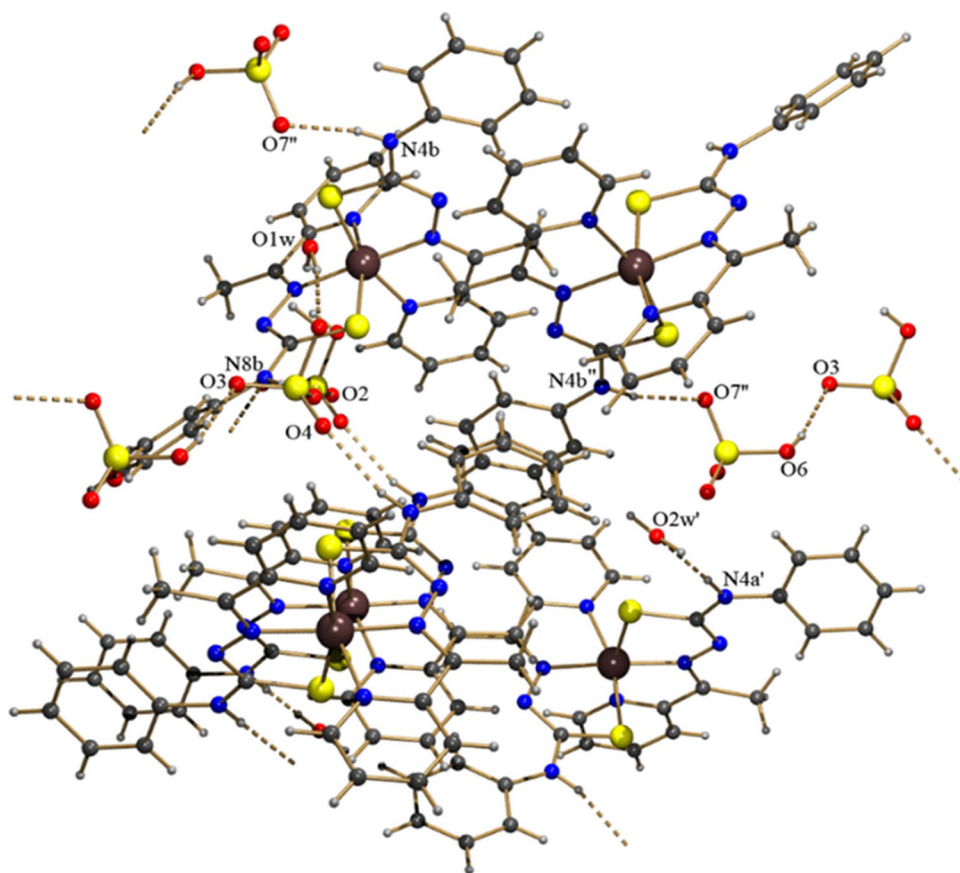


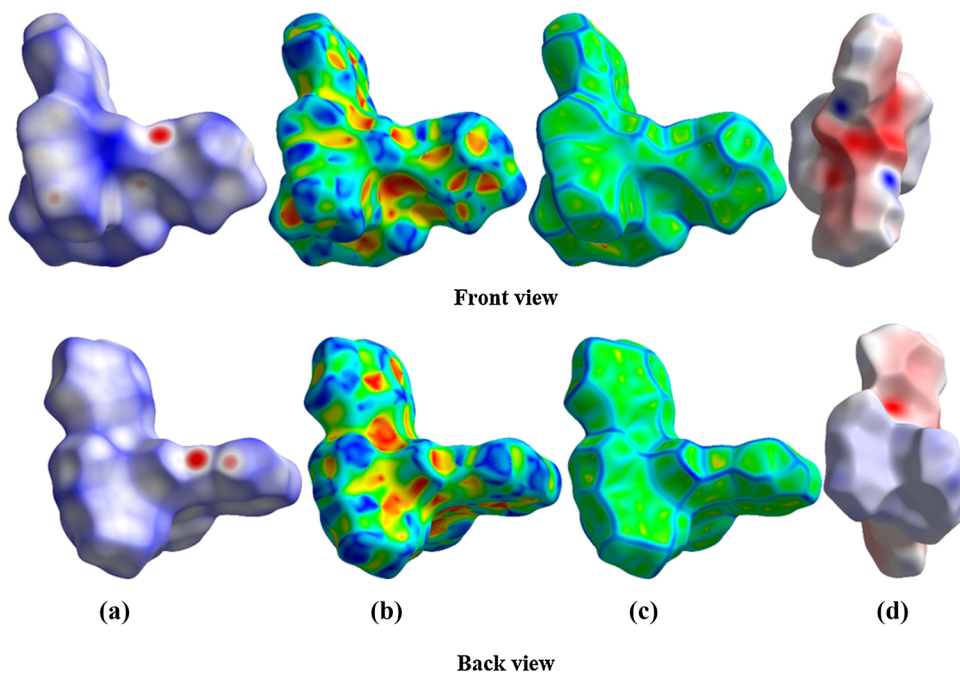
Fig. 6 Crystalline and molecular structure of $2 \cdot \text{H}_2\text{O}$



structure. The crystal structure of $2 \cdot \text{H}_2\text{O}$ was evaluated using d_{norm} , shape index and curvedness, shown in Fig. 7a-c; it investigates the atom \cdots atom interactions. The electrostatic

potential in Fig. 7d shows a large electropositive region (blue) near methyl and pyridine rings (back view) and a large electronegative region (red) near the rings involving

Fig. 7 HS mapped with **a** d_{norm} , **b** shape index, **c** curvedness and **d** electrostatic potential of $2 \cdot \text{H}_2\text{O}$



the S atoms (front view). The positive electrostatic potential occurs because of the contribution of carbon atoms, while the negative electrostatic potential occurs because of the contribution of oxygen, nitrogen and sulphur atoms, which are involved in intra- and intermolecular interactions.

The HS mapped with d_{norm} of $2 \cdot \text{H}_2\text{O}$ in Fig. 8a, b shows one $R_1^2(4)$ and two $R_2^2(8)$ ring motifs. The most intense red regions (stronger interactions) occur near to C–H...O and N–H...O interactions between the compound and hydrogen sulphate ion and between the compound, hydrogen sulphate ion and water.

The analysis about C–H... π interactions of the compound was done using the shape index. In the $2 \cdot \text{H}_2\text{O}$ compound, C–H... π interactions occur between the H atoms with the π -systems, as can be seen in Fig. 9. These interactions are significant to the molecular packing and are consistent with the values found in the percentage of interactions contributions in 2D fingerprint plots.

The 2D fingerprint plots (Fig. 10a–f) are useful for analysing the relative contribution of different intermolecular interactions. The higher contribution of the total HS occurs due to non-classical H...H contacts with 40.3%, as expected for the amount of hydrogen atoms in the molecules. However, the H...O/O...H interactions are the most important contacts for the crystal lattice stability, with a 20.9% contribution to the HS area. Other relevant interactions for the three-dimensional structure are the C...H contacts (equivalent to C–H... π interactions), which contributed to 17.9% to the HS area. It is also necessary to highlight the contributions of N...H/H...N and S...H/H...S in crystal packing, which contribute to 12.8% to the HS area. The inspection of contacts between other atom types pointed out that there are no significant π ... π interactions within the crystals (equivalent to C...C contacts, with 5.1% of the HS area). Figure 11 summarizes the selected percentages of contacts in the crystal structure of $2 \cdot \text{H}_2\text{O}$.

Fig. 8 HS mapped with d_{norm} of $2 \cdot \text{H}_2\text{O}$ to view the **a** $R_1^2(4)$ and **b** $R_2^2(8)$ ring motifs. The surfaces are partially transparent for clarity

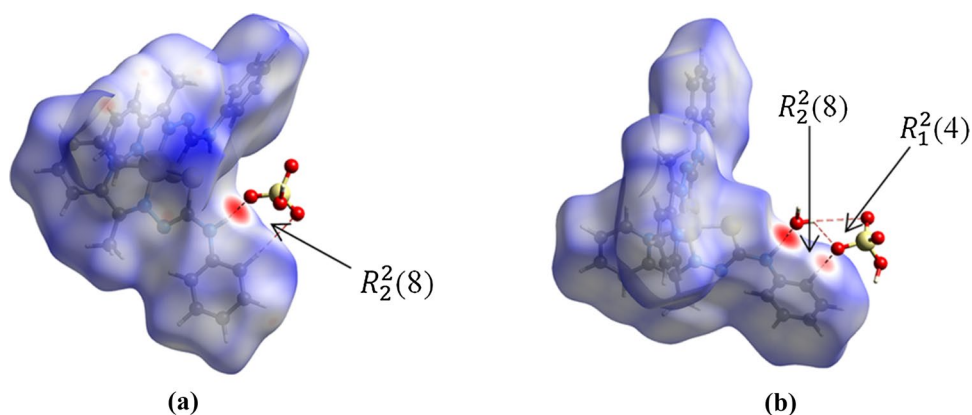


Fig. 9 C–H... π interactions on the HS mapped by the shape index of $2 \cdot \text{H}_2\text{O}$

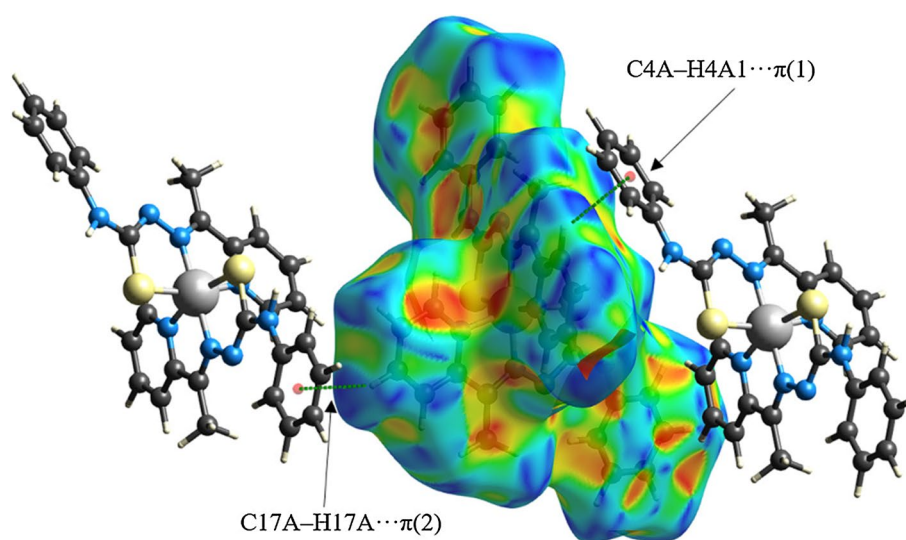
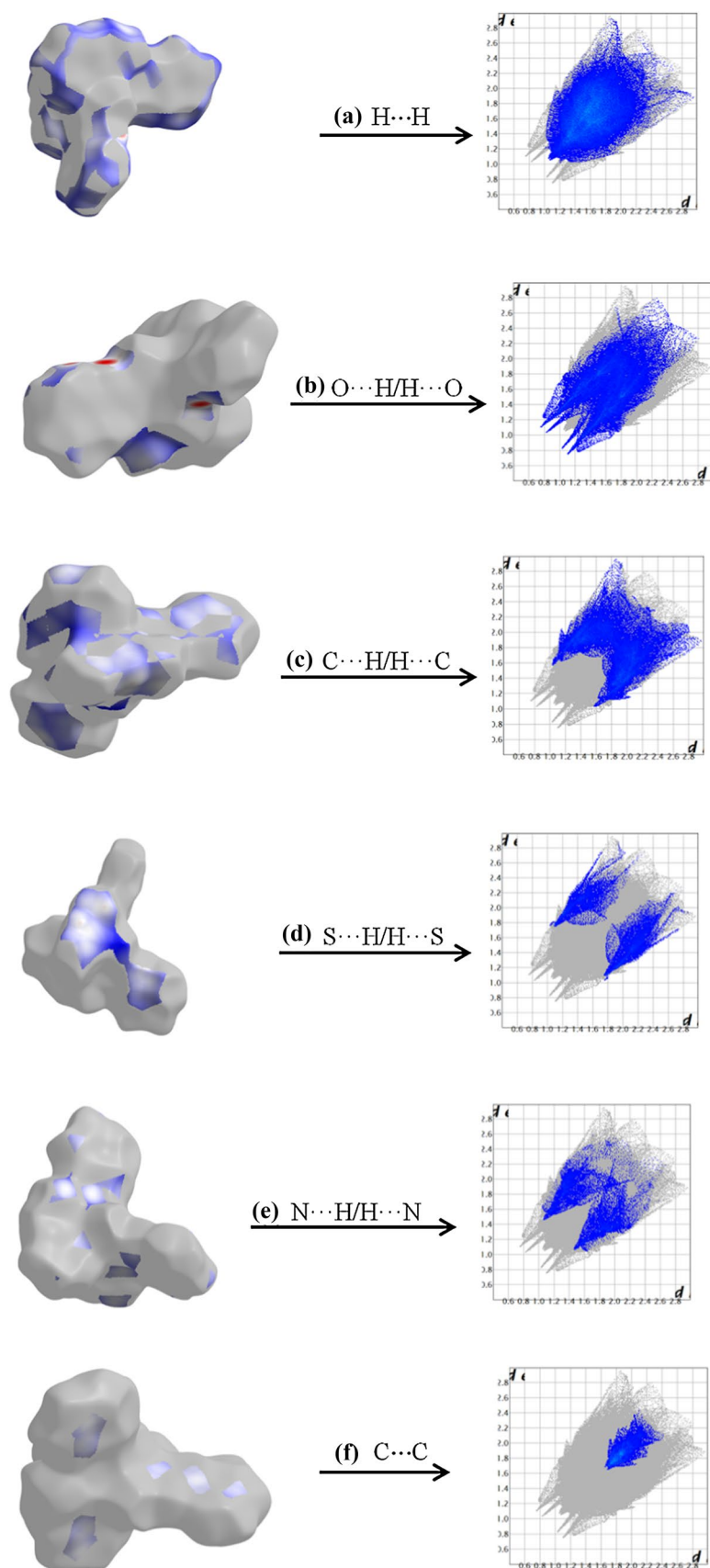


Fig. 10 Decomposed 2D fingerprint plot (in grey) and 2D fingerprint plot of the **a** H···H, **b** O···H/H···O, **c** C···H/H···C, **d** S···H/H···S, **e** N···H/H···N and **f** C···C interactions of 2·H₂O. The *d_i* and *d_e* distance values are shown in Å



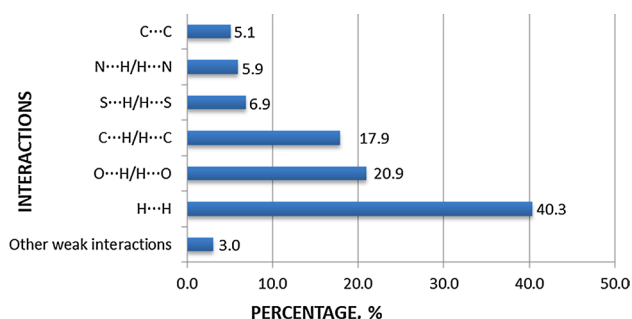


Fig. 11 The percentage contributions selected interaction to the HS area of $2\cdot\text{H}_2\text{O}$

Conclusions

Thiosemicarbazone metal complexes have attracted considerable attention over the past many years due to their significant pharmacological activities and chemical properties, and thus, the study of their structure is important. Based on that, two iron compounds containing thiosemicarbazone as ligands, varying the N(4) substituent group by ethyl and phenyl, were synthesized in satisfactory yields and were characterized both in solution and in the solid state. The complexes adopt a distorted octahedral geometry with the monodeprotonated thiosemicarbazone ligands acting in an *N,N,S* bidentate mode and low-spin ferric centre as confirmed by X-ray analyses. The compound crystallizes in the triclinic crystal system with the space group $P\bar{1}$. Crystallographic analysis of the compound reveals the existence of hydrogen bonds with NH groups and water molecules [$\text{N}(4\text{A})\text{--H}(4\text{A})\cdots\text{O}(2\text{W})$], hydrogen sulphate ions [$\text{O}(6)\text{--H}(6\text{A})\cdots\text{O}(3)$, $\text{O}(6)\text{--H}(6\text{A})\cdots\text{S}(5)$] and molecules of water with hydrogen sulphate ions [$\text{O}(1\text{W})\text{--H}(11\text{W})\cdots\text{S}(2\text{B})$] that contributes to the stability of the crystal structure. Hirshfeld surface analysis revealed that supramolecular structure is stabilized mainly by $\text{H}\cdots\text{H}$, $\text{C}\cdots\text{H}/\text{H}\cdots\text{C}$ and $\text{O}\cdots\text{H}/\text{H}\cdots\text{O}$ interactions, while for $\pi\cdots\pi$ contacts there are no significant contacts in the crystal packing.

Supplementary materials

Supplementary data associated with this article can be found, in the online version, at: Fig. S1: IR spectrum (KBr) of complex $1\cdot\text{H}_2\text{O}$, Fig. S2: IR spectrum (KBr) of complex $2\cdot\text{H}_2\text{O}$, Fig. S3: UV–Vis spectrum of complex **2** in methanolic solution, Fig. S4: intermolecular interactions in the crystalline lattice along the *b* axis of compound $2\cdot\text{H}_2\text{O}$, Table S1: bond lengths (\AA) for complex $2\cdot\text{H}_2\text{O}$, Table S2: additional angles ($^\circ$) for complex $2\cdot\text{H}_2\text{O}$, Table S3: selected torsion angles ($^\circ$) for $2\cdot\text{H}_2\text{O}$, Table S4: hydrogen bonds (\AA , $^\circ$) in crystal structure of $2\cdot\text{H}_2\text{O}$, Table S4 hydrogen bonds (\AA , $^\circ$) in crystal structure of $2\cdot\text{H}_2\text{O}$. Details on data collection, refinement

and crystallographic data in CIF format for structure $[\text{Fe}(\text{atc-Ph})_2]\text{HSO}_4\cdot\text{H}_2\text{O}$ have been deposited at the Cambridge Crystallographic Data Centre CCDC 1990298. Copies of this information may be obtained free of charge from The Director, CCDC, 12 Union Road, Cambridge, CB21EZ, UK (fax: +44 1223 336 033 ; email: deposit@ccdc.cam.ac.uk or [www: http://www.ccdc.cam.ac.uk](http://www.ccdc.cam.ac.uk)).

Acknowledgements This work was supported by Fundação de Amparo à Pesquisa do Estado de São Paulo/FAPESP; Conselho Nacional de Pesquisa/CNPq; and Fundação de Amparo à Pesquisa de Minas Gerais/FAPEMIG. This study was financed in part by the Coordenação de Aperfeiçoamento de Pessoal de Nível Superior—Brasil (CAPES)—Finance Code 001. The researchers would like to thank the Multi-user Laboratory of Institute of Chemistry of Federal University of Uberlândia for the NMR analysis. The authors would also like to thank Samuel Carlos Silva and professor Edson Nossol from Group of Nanostructured and Inorganic Chemistry Materials at Federal University of Uberlândia for electrochemistry analysis.

Funding FAPESP (Grant 2009/54011-8), CAPES and CNPq.

Compliance with ethical standards

Conflicts of interest The authors declare no conflict of interest.

References

- Hazra M, Dolai T, Pandey A, Dey SK, Patra A (2014) *Bioinorg Chem Appl* 2014(104046):13p. <https://doi.org/10.1155/2014/104046>
- Yam VWW, Wong KMC (2011) *Chem Commun* 47:11579–11592. <https://doi.org/10.1039/C1CC13767K>
- Sathish V, Ramdass A, Velayudham M, Lu KL, Thanasekaran P, Rajagopal S (2017) *Dalton Trans* 46(48):16738–16769. <https://doi.org/10.1039/C7DT02790G>
- Shen X, Chen X, Chen J, Sun Y, Cheng Z, Lu Z (2020) *Nature Communications* 783:1–8. <https://doi.org/10.1038/s41467-020-14459-x>
- Rorabacher DB (2004) *Chem Rev* 104(2):651–698. <https://doi.org/10.1021/cr020630e>
- Humphreys KJ, Karlin KD, Rokita SE (2002) *J Am Chem Soc* 124(27):8055–8066. <https://doi.org/10.1021/ja012539i>
- Adam FI, Bounds PL, Kissner R, Koppenol WH (2015) Redox properties and activity of iron-citrate complexes: evidence for redox cycling. *Chem Res Toxicol* 28(4):604–614
- Arion VB (2019) *Coord Chem Rev* 387:348–397. <https://doi.org/10.1016/j.ccr.2019.02.013>
- Netalkar PP, Netalkar SP, Revankar VK (2015) *Polyhedron* 100:215–222. <https://doi.org/10.1016/j.poly.2015.07.075>
- Quiroga AG, Ranninger CN (2004) *Coord Chem Rev* 248(1):119–133. <https://doi.org/10.1016/j.cc.2003.11.004>
- Oliveira CG, Maia PIS, Souza PC, Pavan FR, Leite CQF, Viana RB, Batista AA, Nascimento OR, Deflon VM (2014) *J Inorg Biochem* 132:21–29. <https://doi.org/10.1016/j.jinorgbio.2013.10.011>
- Santoro A, Vileno B, Palacios O, Peris-Díaz MD, Riegel G, Gaiddon C, Krężel A, Faller P (2019) *Metallomics* 11(5):994–1004. <https://doi.org/10.1039/C9MT00061E>
- Lopes EO, Oliveira CG, Silva PB, Eismann CE, Suárez CA, Menegário AA, Leite CQF, Deflon VM, Pavan FR (2016) *Int J Mol Sci* 781:1–15. <https://doi.org/10.3390/ijms17050781>

14. Oliveira CG, Maia PIS, Miyata M, Pavan FR, Leite CQF, Almeida ET, Defflon VM (2014) *J Braz Chem Soc* 25(10):1848–1856. <https://doi.org/10.5935/0103-5053.20140149>
15. Oliveira CG, Romero-Canelón I, Silva MM, Coverdale JPC, Maia PIS, Batista AA, Castelli S, Desideri A, Sadler PJ, Defflon VM (2019) *Dalton Trans* 48(44):16509–16517. <https://doi.org/10.1039/c9dt02570g>
16. Arancibia R, Quintana C, Biot C, Medina ME, Carrère-Kremer S, Kremer L, Klahn AH (2015) *Inorg Chem Commun* 55:139–142. <https://doi.org/10.1016/j.inoche.2015.03.036>
17. Tavares TT, Paschoal D, Motta EVS, Carpanez AG, Lopes MTP, Fontes ES, Santos HF, Silva H, Grazul RM, Fontes APS (2014) *J Coord Chem* 67(6):956–968. <https://doi.org/10.1080/0095872.2014.900664>
18. Lu S, Chiang JC, Chiou TW, Liaw WF (2019) *J Chin Chem Soc* 66(9):1186–1194. <https://doi.org/10.1002/jccs.201900147>
19. Wei D, Netkaew C, Darcel C (2019) *Eur J Inorg Chem* 2019(20):2471–2487. <https://doi.org/10.1002/ejic.201900122>
20. Fu Z, Chen R (2019) *J Anal Met Chem* 2019(3894571):1–6. <https://doi.org/10.1155/2019/3894571>
21. Richardson DR, Sharpe PC, Lovejoy DB, Senaratne D, Kalinowski DS, Islam M, Bernhardt PV (2006) *J Med Chem* 49(22):6510–6521. <https://doi.org/10.1021/jm0606342>
22. Atasever B, Ulkuseven B, Bal-Demirci T, Erdem-Kuruca S, Solakoglu Z (2010) *Invest New Drugs* 28:421–432. <https://doi.org/10.1007/s10637-009-9272-2>
23. Tarallo MB, Urquiola C, Monge A, Costa BP, Ribeiro RR, Costa-Filho AJ, Mercader RC, Pavan FR, Leite CQF, Torre MH, Gambino D (2010) *J Inorg Biochem* 104(11):1164–1170. <https://doi.org/10.1016/j.jinorgbio.2010.07.005>
24. Serda M, Kalinowski DS, Mrozek-Wilczkiewicz A, Musiol R, Szurko A, Ratuszna A, Pantarat N, Kovacevic Z, Merlot AM, Richardson DR, Polanski J (2012) *Bioorg Med Chem Lett* 22(17):5527–5531. <https://doi.org/10.1016/j.bmcl.2012.07.030>
25. Soares MA, Lessa JA, Mendes IC, Silva JG, Santos RG, Salum LB, Daghestani H, Andricopulo AD, Day BW, Vogt A, Pesquero JL, Rocha WR, Beraldo H (2012) *Bioorg Med Chem* 20(11):3396–3409. <https://doi.org/10.1016/j.bmc.2012.04.027>
26. Earnshaw A (1968) *Introduction to magnetochemistry*, 1st edn. Academic Press, New York
27. Kahn O (1993) *Molecular magnetism*, 1st edn. VCH Publishers Inc, New York
28. Richardson DR, Kalinowski DS, Richardson V, Sharpe PC, Lovejoy DB, Islam M, Bernhardt PV (2009) *J Med Chem* 52(5):1459–1470. <https://doi.org/10.1021/jm801585u>
29. Sheldrick GM (2008) *Acta Crystallogr A* 64(Pt 1):112–122. <https://doi.org/10.1107/S0108767307043930>
30. Sheldrick GM (2015) *Acta Cryst. C* 71(1):3–8. <https://doi.org/10.1107/S2053229614024218>
31. Macrae CF, Edgington PR, McCabe P, Pidcock E, Shields GP, Taylor R, Towler M, Van de Streek J (2006) *J Appl Cryst* 39(3):453–457. <https://doi.org/10.1107/S002188980600731X>
32. Wolff SK, Grimwood DJ, McKinnon JJ, Jayatilaka D, Spackman MA, Tuner MJ, Spackman PR (2017) *Crystal explorer 17.5*. University of Western Australia, Perth
33. Yu Y, Kalinowski DS, Kovacevic Z, Siafakas AR, Jansson PJ, Stefani C, Lovejoy DB, Sharpe PC, Bernhardt PV, Richardson DR (2009) *J Med Chem* 52(17):5271–5294. <https://doi.org/10.1021/jm900552r>
34. Nakamoto K (2009) *Infrared and Raman spectra of inorganic and coordination compounds, part b: applications in coordination, organometallic, and bioinorganic chemistry*, 6th edn. Wiley, New York
35. da Maia PIS, Carneiro ZA, Lopes CD, Oliveira CG, Silva JS, Albuquerque S, Hagenbach A, Gust R, Defflon VM, Abram U (2017) *Dalton Trans* 46(8):2559–2571. <https://doi.org/10.1039/C6DT04307K>
36. Goncalves ACR, Carneiro ZA, Oliveira CG, Danuello A, Guerra W, Oliveira RJ, Ferreira FB, Veloso-Silva LLW, Batista FAH, Borges JC, de Albuquerque S, Defflon VM, Maia PIS (2017) *Eur J Med Chem* 141:615–631. <https://doi.org/10.1016/j.ejmech.2017.10.013>
37. Graminha AE, Vilhena FS, Batista AA, Louro SRW, Ziolli RL, Teixeira LR, Beraldo H (2008) *Polyhedron* 27(2):547–551. <https://doi.org/10.1016/j.poly.2007.10.008>
38. Jain SK, Garg BS, Bhoon YK (1986) *Transition Met Chem* 11(3):89–95. <https://doi.org/10.1007/BF00623761>
39. Borges RH, Paniago E, Beraldo H (1997) *J Inorg Biochem* 65(4):267–275. [https://doi.org/10.1016/s0162-0134\(96\)00142-0](https://doi.org/10.1016/s0162-0134(96)00142-0)
40. West DX, Ahrweiler PM, Ertem G, Scovill JP, Klayman DL, Flippen-Anderson JL, Gilardi R, George C, Pannell LK (1985) *Transition Met Chem* 10(7):264–270. <https://doi.org/10.1007/BF00621084>
41. Saha R, Biswas S, Steele IM, Dey K, Mostafa G (2011) *Dalton Trans* 40(13):3166–3175. <https://doi.org/10.1039/C0DT01256D>
42. Zhao Y, Shen XF, Zhang LF (2018) *Acta Crystallogr E Crystallogr Commun* 74(Pt 2):252–255. <https://doi.org/10.1107/S2056989018001263>
43. Etter MC (1990) *Acc Chem Res* 23(4):120–126. <https://doi.org/10.1021/ar00172a005>

Publisher's Note Springer Nature remains neutral with regard to jurisdictional claims in published maps and institutional affiliations.